

Dynamic Modeling and Response Analysis of an Optical Machining Robot with Prismatic Joint Clearance

Zhu, Shuaishuai ; Cheng, Gang; Guo, Feng; Pang, Y.

DOI

[10.3390/app15063197](https://doi.org/10.3390/app15063197)

Publication date

2025

Document Version

Final published version

Published in

Applied Sciences

Citation (APA)

Zhu, S., Cheng, G., Guo, F., & Pang, Y. (2025). Dynamic Modeling and Response Analysis of an Optical Machining Robot with Prismatic Joint Clearance. *Applied Sciences*, 15(6), Article 3197.
<https://doi.org/10.3390/app15063197>

Important note

To cite this publication, please use the final published version (if applicable).
Please check the document version above.

Copyright

Other than for strictly personal use, it is not permitted to download, forward or distribute the text or part of it, without the consent of the author(s) and/or copyright holder(s), unless the work is under an open content license such as Creative Commons.

Takedown policy

Please contact us and provide details if you believe this document breaches copyrights.
We will remove access to the work immediately and investigate your claim.

Article

Dynamic Modeling and Response Analysis of an Optical Machining Robot with Prismatic Joint Clearance

Shuaishuai Zhu ^{1,2}, Gang Cheng ^{1,*}, Feng Guo ³ and Yusong Pang ⁴¹ School of Mechatronic Engineering, China University of Mining and Technology, Xuzhou 221116, China; zhuss@cumt.edu.cn² School of Intelligent Manufacturing and Emergency Equipment, Jiangsu College of Safety Technology, Xuzhou 221004, China³ School of Mechanical and Electrical Engineering, Xuzhou University of Technology, Xuzhou 221018, China; gfeng@xzit.edu.cn⁴ Faculty of Mechanical Engineering, Delft University of Technology, 2628 Delft, The Netherlands; y.pang@tudelft.nl

* Correspondence: chg@cumt.edu.cn

Featured Application: The proposed clearance contact model and dynamic modeling method can be used not only for the dynamic control of polishing robots, but also for planar or spatial robots with different topological structures.

Abstract: The accuracy and stability of robotic systems are significantly influenced by joint clearances, especially in precision applications like optical mirror polishing. This study focuses on a 5-DOF (Degree of Freedom) parallel manipulator designed for optical mirror polishing. The study conducts dynamic modeling by incorporating prismatic joint clearance and examines the resulting dynamic response. Previous studies on dynamic modeling have primarily focused on planar mechanisms with rotational or ball joint clearances, whereas research on parallel manipulators with spatial prismatic joint clearances remains limited. This study introduces a comprehensive dynamic modeling framework for parallel manipulators with prismatic joint clearance, utilizing the Lagrange multiplier method (LMD). First, the prismatic joint models of the guideway and slider in the parallel manipulator are simplified, enabling the determination of different contact states and the calculation of friction and contact forces for various contact types. Second, the dynamic equations of the parallel manipulator are derived by establishing system constraint equations. Finally, the dynamic responses of various clearance-related factors are determined through a combination of theoretical calculations and ADAMS simulations. This study provides a framework for modeling the dynamics of parallel manipulators with prismatic joint gaps, offering valuable insights into the design and control of high-precision robotic systems.

Keywords: parallel manipulator; dynamic model; prismatic joint clearance; LMD

Academic Editors: Abdessattar Abdelkefi, Daniil Yurchenko and Riadh Elleuch

Received: 29 January 2025

Revised: 12 March 2025

Accepted: 13 March 2025

Published: 14 March 2025

Citation: Zhu, S.; Cheng, G.; Guo, F.; Pang, Y. Dynamic Modeling and Response Analysis of an Optical Machining Robot with Prismatic Joint Clearance. *Appl. Sci.* **2025**, *15*, 3197. <https://doi.org/10.3390/app15063197>

Copyright: © 2025 by the authors. Licensee MDPI, Basel, Switzerland. This article is an open access article distributed under the terms and conditions of the Creative Commons Attribution (CC BY) license (<https://creativecommons.org/licenses/by/4.0/>).

1. Introduction

Optical processing robots, particularly in the field of optical mirror polishing, have garnered significant attention in recent years. Due to their high mechanical precision and stability, optical machining robots are also employed in high-tech industries such as aerospace, military, and semiconductor manufacturing [1]. In precision operations, these robots must operate within an extremely small error range to ensure the final product's

quality. With ongoing technological advancements, optical processing robots have evolved from traditional single-degree-of-freedom manipulators to multi-degree-of-freedom parallel robots, offering greater flexibility and finer control [2]. However, as the DOFs (degrees of freedom) have increased, clearance issues between the robot's joints have emerged, becoming a critical factor affecting its dynamic response, accuracy, and stability [3,4].

Joint clearance has a very pronounced effect on the kinematic and dynamic performance of a robot. Several studies have employed hybrid contact force models to simulate the dynamic behavior of joint clearances. Li et al. [5] simulated a crank-slider mechanism with multi-clearance joints utilizing a nonlinear contact force model for joint internal force assessment. Ren [6] derived the dynamic equations of a four-bar mechanism with a gap in a microgravity environment and demonstrated experimentally that the gap reduces the accuracy of the mechanism's motion. Friction factors of gap size, relative velocity, and material between moving joints can significantly affect the dynamic response and lead to chaotic behavior [7]. Current research on joint clearance effects primarily focuses on planar or connecting rod mechanisms, where the analyzed clearance typically involves only two-dimensional contact, lacking comprehensive spatial contact collision analysis.

Joint clearance in spatial mechanisms significantly impacts their dynamic performance. Erkaya [8] studied a spatial slider-crank mechanism and found joint clearance caused chaotic kinematic and dynamic responses. Chen et al. [9] compare the effects of different frictional contact models on the dynamical properties of space mechanisms. N. Cretescu et al. [10] studied the impacts of clearance, friction, and rod flexibility on a Delta robot through simulation. Wang [11] modeled the dynamics of a compound swing jaw crusher with a gap and investigated the effects of driving speed on the dynamic of the crusher. Wang [12] examined joint clearance in a wine box base assembly robot, formulating the dynamic equation and studying its impact, finding that larger gap sizes affect the end-effector's dynamic performance. Current research has predominantly focused on the contact collision modeling of ball and rotational joint gaps, whereas studies on prismatic joint gaps remain limited.

Prismatic joints are prevalent in multibody systems, and contact detection is crucial for understanding and optimizing the system's dynamic behavior. Qian [13] designed a planar clearance-containing mechanism, analyzed basic methods of gap joints, and studied the mechanism's dynamic characteristics via experiments and simulations. Qi [14] simplified the contact pattern of spatial prismatic joints by introducing a gap function. T. N. [15] considered joint flexibility, clearance, and friction in a 3-PRS series mechanism, finding that increased joint clearance and friction coefficient raise joint contact forces, affecting the dynamic response and natural frequency. Qian et al. [16] classified the contact patterns in translational joints and proposed a method for contact pattern recognition in planar mechanisms. Most existing studies on the impact of joint gaps on mechanism dynamics have concentrated on spatial prismatic joints within linkage mechanisms.

To the best of our knowledge, research on prismatic joint clearance for space-parallel robots with multiple DOFs and complex structures remains highly limited. This study focuses on a polishing robot with joint clearance as the research object, analyzing the dynamic characteristics of the mechanism through theoretical modeling and computer simulations.

The paper is organized as follows. Section 2 outlines the contact modes of spatial prismatic joints, which include 18 point–line–surface contact configurations. Section 3 presents the dynamic model of the 3-UPRU+UP parallel manipulator, incorporating prismatic joint clearance. Section 4 provides the numerical results of the dynamic model, analyzing the effects of different clearance sizes and friction factors. Section 5 discusses the findings and the implications. Finally, Section 6 presents the conclusions of the study.

2. Modeling of Spatial Prismatic Joint Clearance

The polishing robot, as shown in Figure 1a, consists of three active branches, UPRU (Universal joint—Prismatic joint—Rotational joint—Universal joint), and a constraint branch UP (Universal joint—Prismatic joint). Point U_i ($i = 1, 2, 3$) is on the static platform, and Point U_k ($k = 5, 6, 7$) is on the moving platform. The length of the cylinder block components is $L_{a,i}$, and the mass is $m_{a,i}$; the length of the telescopic rod components is $L_{b,i}$, and the mass is $m_{b,i}$; the length of the rotating rods is $L_{c,i}$, and the mass is $m_{c,i}$. The UP branch chain is rigidly connected to the moving platform and is treated as a single component with a mass of m_m . The coordinate system, shown in Figure 1b, is established, where W -XYZ represents the world coordinate system. The origin of the static coordinate system is placed at S_0 , which is the center of the static platform. $\overrightarrow{S_0U_3}$ and $\overrightarrow{U_1U_2}$ are the x -axis and y -axis positive directions, respectively, of the local coordinate system S_0 -xyz, and the right-hand rule determines the z -axis. The origin of the moving platform coordinate system is placed at M_0 , with the positive direction of x_0 axis aligning with $\overrightarrow{M_0U_7}$, and the positive direction of y_0 aligning with $\overrightarrow{U_5U_6}$. Define the joint local coordinate system a_i -xyz, b_j -xyz, and c_i -xyz at the centers of mass of the cylinder assembly, telescopic rod assembly, UP branch chain, and rotating assembly, respectively.

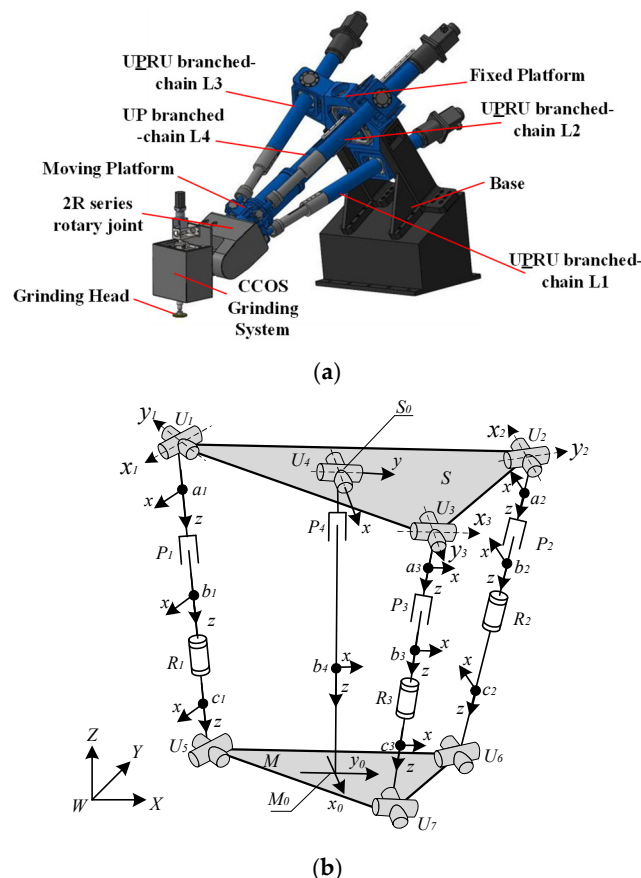


Figure 1. Hybrid processing robot: (a) 3D structure, (b) schema.

2.1. Contact Mode Description

The prismatic joint in the UP branched-chain, as shown in Figure 2a, consists of two components: the slide and the guide rail. Let the guide rail be denoted as L and the slide as K , and define coordinate systems $O^l - e_1^l e_2^l e_3^l$, $O^k - e_1^k e_2^k e_3^k$ at the centers of mass of the guide rail and the slide. When L is in contact with K , the contact between the two can be

determined by the relative position of the surface points. A simplified model of the guide and slider is shown in Figure 2b.

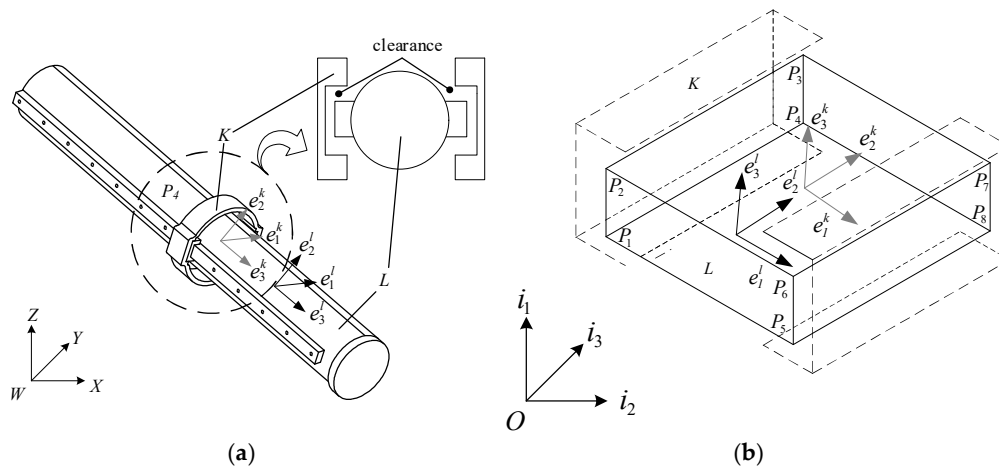


Figure 2. Prismatic joint in UP branch chain: (a) structure, (b) simplified model.

Due to the presence of prismatic joint gaps, the guideway and the slider are subject to different contact patterns, each corresponding to a different attitude. By calculating the positions and velocities of points P_1 – P_8 , the contact state between the track and the slider can be obtained.

ξ^l and ξ^k are the position vectors of the center of mass of L and K in $O-i_1i_2i_3$, respectively. Let the vectors between the two center of mass coordinate systems be $\overrightarrow{OO^k} = \mathbf{q}$, $\overrightarrow{OP_1} = \mathbf{p}_1$, and $\overrightarrow{OP_1} = \mathbf{P}_1$, and the position vectors of point P_1 in $O^l - e_1^l e_2^l e_3^l$ and $O^k - e_1^k e_2^k e_3^k$ coordinate systems are \mathbf{r}_1^l and \mathbf{R}_1^k respectively. T_l and T_k are the coordinate transformation matrices of L and K relative to the coordinate system $O-i_1i_2i_3$. The following, Equation (1), can be derived from the closed-loop vector relationship:

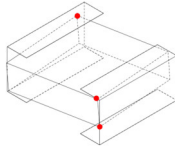
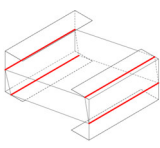
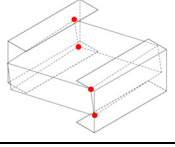
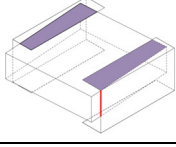
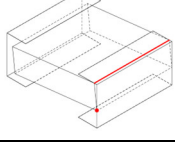
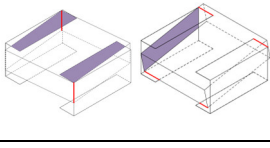
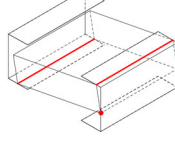
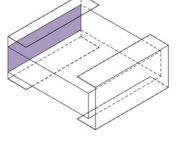
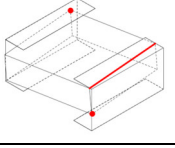
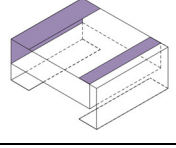
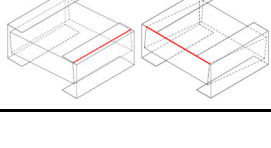
$$\begin{cases} \mathbf{R}_1^k = -\mathbf{q} + \mathbf{p}_1 = \xi^l - \xi^k + T_l \mathbf{r}_1^l \\ \mathbf{R}_1^k = A_k^T \mathbf{P}_1 = A_k^T (\xi^l - \xi^k + T_l \mathbf{r}_1^l) \end{cases} \quad (1)$$

When $\mathbf{R}_1^k \cdot \mathbf{e}_1^k > a'/2$, point P_1 contacts the upper surface, and when $\mathbf{R}_1^k \cdot \mathbf{e}_2^k > b'/2$, point P_1 contacts the side surface. The relative position vector of P_1 is $\dot{\delta} = \dot{\mathbf{R}}_1^k$. The normal contact force between two objects in contact acts in a direction is \mathbf{e}_1^k or \mathbf{e}_2^k . Similarly, the contact mode of points P_1 – P_8 can be obtained.

Table 1 provides a summary of the identified contact modes.

Table 1. Contact mode of the prismatic joint.

Order	Diagram	Description	Order	Diagram	Description
1		Single point of contact	9		Double lines of contact
2		Double points of contact	10		Three lines of contact

3		Three points of contact	11		Four lines of contact
4		Four points of contact	12		Single line and single plane of contact
5		Single point and single line of contact	13		Double lines and single plane of contact
6		Single point and double lines of contact	14		One plane of contact
7		Double points and single line of contact	15		Two planes of contact
8		Single line of contact			

2.2. Contact Force Calculation Under Different Contact Modes

Due to the clearance, during the motion of the mechanism, the contact surfaces of the two elements will experience friction and wear, leading to high temperatures. Ignoring factors such as wear and lubrication, the contact forces between L and K are the normal force (F_N) and the tangential force (F_T). Depending on the type of contact between the two, the calculation of normal force is divided into the following three types:

2.2.1. Contact Force Calculation for Plane Contact

After calculating F_N , F_T can be determined using the Coulomb friction model. F_T is shown as follows:

$$F_T = \mu F_N \quad (2)$$

where μ represents the coefficient of sliding friction.

Since the Coulomb friction model cannot describe the relationship between friction over time, a dynamic friction coefficient based on the change in velocity is used to more accurately describe the friction process [17].

$$\mu = \begin{cases} \mu_d & |V| > V_d \\ \mu_s \sin\left(\frac{\pi}{2} \frac{|V|}{V_s}\right) & |V| < V_s \\ \frac{(\mu_s + \mu_d)}{2} + \frac{1}{2} \left[(\mu_s - \mu_d) \cos\left(\pi \frac{|V| - V_s}{V_d - V_s}\right) \right] & V_s \leq |V| \leq V_d \end{cases} \quad (3)$$

where V_s and V_d represent the velocities for transitions from stick-slip and static-to-sliding friction; μ_s and μ_d represent the coefficients of static friction and sliding friction, respectively.

The slider and the guideway form a rectangular contact area. The $F_N(\delta)$ between the slider and the guideway can be expressed as follows [18]:

$$F_N(\delta) = \frac{EA\delta'}{l} \quad (4)$$

where E represents the material's elastic modulus, A denotes the area of the contact part, δ indicates the compression depth, and l corresponds to the material's thickness along the primary compression axis.

2.2.2. Contact Force Calculation for Line Contact

In the line contact, the contact surfaces have rectangular contact areas, and this interaction is known as cylindrical contact. The contact forces are distributed in a cylinder as described below [19]:

$$F(x) = \frac{2P}{\pi a^2 b} \sqrt{a^2 - x^2} \quad (5)$$

where x is the perpendicular distance; a and b are the width and length of the contact area, respectively; P denotes the pressure per unit length; R is the equivalent radius of curvature; and the penetration depth δ is as follows [20]:

$$\delta = \frac{P}{\pi E^* l} \left[1 - \ln\left(\frac{PR}{\pi E^* l^3}\right) \right] \quad (6)$$

2.2.3. Contact Force Calculation for Point Contact

In the point contact mode, the F_N can be obtained from the L-N contact model [21]:

$$F_N = K \delta^e + D \dot{\delta} \quad (7)$$

where K represents the Hertzian contact stiffness, D denotes the damping coefficient, δ indicates the penetration depth, and $\dot{\delta}$ denotes the relative velocity.

3. Dynamic Modeling of 3-UPRU+UP with Prismatic Joint Clearance

3.1. Dynamic Modeling with Ideal Joints

The polishing robot has a topological configuration of 3-UPRU+UP. The spatial mechanism consists of 10 active components, as shown in Figure 1b. Each active component is characterized by six independent motion parameters within the W-XYZ. The generalized coordinates of all active components are expressed as follows:

$$\mathbf{q} = \left[q_{a,1} \quad q_{a,2} \quad q_{a,3} \quad q_{b,1} \quad q_{b,2} \quad q_{b,3} \quad q_{c,1} \quad q_{c,2} \quad q_{c,3} \quad q_m \right]_{60 \times 1}^T \quad (8)$$

The system constraint equations encapsulate the limitations imposed by all constituent joints and ideal actuators. These constraints restrict the relative movement between adjacent rigid bodies and are described through the relationships between vectors on these bodies. The 3-UPRU+UP polishing robot features four kinds of joint: U, P, R, and composite UP joint, along with three actuators. Consequently, 60 independent constraint equations must be established. The formulation of these constraint equations for the specified joints and actuators is as follows.

3.1.1. Constraint Equation of the U-Joint

Figure 3 shows the constraint vector of the U-joint. The U-joint has two DOFs, which limit the motion of the attached rigid body in four directions, forming four independent constraint equations. The dotted line represents the two orthogonal rotation axes of the U-joint, and point P is the center point. \mathbf{r}_i and \mathbf{r}_j are the position vectors of the two rigid bodies connected by the U-joint in O_W -XYZ; \mathbf{o}_i^p and \mathbf{o}_j^p represent the position vectors of point P in the U-joint in o_i - $x_i y_i z_i$ and o_j - $x_j y_j z_j$, respectively; \mathbf{d}_{oi} and \mathbf{d}_{oj} are unit vectors fixed to rigid bodies i and j along the rotational axes of the U-joint, respectively. During the motion process, \mathbf{d}_{oi} must always be perpendicular to \mathbf{d}_{oj} , and the constraint equation of the U-joint is as follows:

$$\Phi_U = \begin{bmatrix} \mathbf{r}_i + \mathbf{R}_i \mathbf{o}_i^p - \mathbf{r}_j - \mathbf{R}_j \mathbf{o}_j^p \\ (\mathbf{R}_i \mathbf{d}_{oi})^T (\mathbf{R}_j \mathbf{d}_{oj}) \end{bmatrix} = \mathbf{0}_{4 \times 1} \quad (9)$$

where \mathbf{R}_i and \mathbf{R}_j are the rotation matrix from o_i - $x_i y_i z_i$ and o_j - $x_j y_j z_j$ to W -XYZ, respectively.

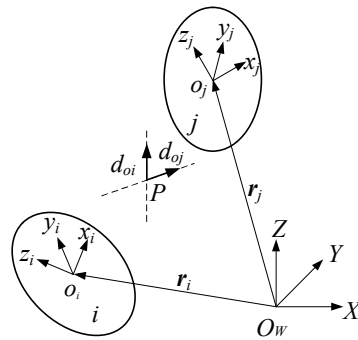


Figure 3. Constraint vector of the U-joint.

3.1.2. Constraint Equation of the P-Joint

The P-joint has one DOF, which forms five independent constraint equations. The constraint vector diagram of the prismatic joint is shown in Figure 4, where the dotted line denotes the moving axis. Establish a local coordinates system on the two rigid bodies connected by prismatic joints, where z_i and z_j are parallel to the moving axis. \mathbf{d}_{xi} , \mathbf{d}_{yi} , and \mathbf{d}_{zi} are unit vectors fixed on rigid body i , with \mathbf{d}_{zi} parallel to the moving axis; \mathbf{d}_{xj} , \mathbf{d}_{yj} , and \mathbf{d}_{zj} are unit vectors fixed on rigid body j , with \mathbf{d}_{zj} parallel to the moving axis; point P is on the moving axis of rigid body i , and point Q is on the moving axis of rigid body j . During motion, the line connecting P and Q is always parallel to \mathbf{d}_{zj} , which means, $\overline{PQ} \perp \mathbf{d}_{xi}$, $\overline{PQ} \perp \mathbf{d}_{yi}$. Simultaneously, $\mathbf{d}_{xi} \perp \mathbf{d}_{zj}$, $\mathbf{d}_{yi} \perp \mathbf{d}_{zj}$, $\mathbf{d}_{xi} \perp \mathbf{d}_{yj}$. The constraint equation for the P-joint can be expressed as:

$$\Phi_P = \begin{bmatrix} (\mathbf{R}_i \mathbf{d}_{xi})^T \overline{QP}_i \\ (\mathbf{R}_i \mathbf{d}_{yi})^T \overline{QP}_i \\ (\mathbf{R}_j \mathbf{d}_{yj})^T (\mathbf{R}_i \mathbf{d}_{xi}) \\ (\mathbf{R}_j \mathbf{d}_{zj})^T (\mathbf{R}_i \mathbf{d}_{yi}) \\ (\mathbf{R}_j \mathbf{d}_{xj})^T (\mathbf{R}_i \mathbf{d}_{zi}) \end{bmatrix} = \mathbf{0}_{5 \times 1} \quad (i = 1, 2, 3; j = 1, 2, 3) \quad (10)$$

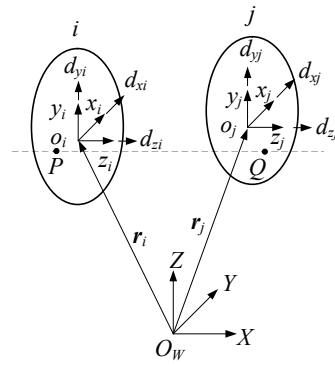


Figure 4. Constraint vector of the P-joint.

3.1.3. Constraint Equation of the R-Joint

The R-joint has one DOF, which restricts relative rotation in two directions and relative movement in three directions between the two connected rigid bodies, resulting in five independent constraint equations. The constraint vector diagram of the R-joint is shown in Figure 5. Rigid bodies i and j form a rotational joint at point P/Q . The dotted line represents the rotation axis. Establish a local coordinates system on the two rigid bodies connected by rotational joints, where z_i and z_j are parallel to the rotation axis. d_{xi} , d_{yi} , and d_{zi} are unit vectors fixed on rigid body i , with d_{zi} parallel to the rotation axis; d_{xj} , d_{yj} , and d_{zj} are unit vectors fixed on rigid body j , with d_{zj} parallel to the rotation axis. During motion, due to the motion characteristics of the rotational joint, d_{zi} is always perpendicular to d_{xj} and d_{yj} . Points P and Q remain coincident. The constraint equation for the R-joint is as follows:

$$\Phi_R = \begin{bmatrix} \mathbf{r}_i + \mathbf{R}_i \mathbf{o}_i^P - \mathbf{r}_j - \mathbf{R}_j \mathbf{o}_j^P \\ (\mathbf{R}_i \mathbf{d}_{zi})^T (\mathbf{R}_j \mathbf{d}_{xj}) \\ (\mathbf{R}_i \mathbf{d}_{zi})^T (\mathbf{R}_j \mathbf{d}_{yj}) \end{bmatrix} = \mathbf{0}_{5 \times 1} \quad (11)$$

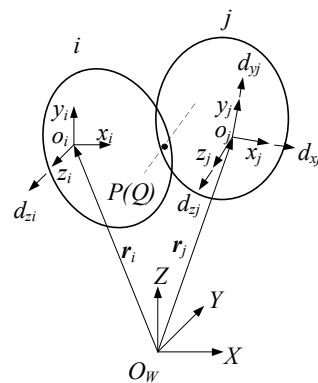


Figure 5. Constraint vector of the R-joint.

3.1.4. Constraint Equation of the Composite UP Joint

The composite UP joint has three DOFs, which restricts relative rotation in one direction and relative movement in two directions between the two connected rigid bodies, resulting in three independent constraint equations. Figure 6 shows the constraint vector diagram of the composite UP joint. Points P and Q are the centers of the static and moving platforms, respectively. The dotted line represents the moving axis of the P-joint; d_{oi} and d_{oj} are the rotation axis of the U-joint. During motion, the line connecting P and Q is always perpendicular to d_{oi} and d_{oj} on the moving platform. Simultaneously, d_{oi} and d_{oj} are

perpendicular to each other. The constraint equation for the composite universal and prismatic joint can be expressed as:

$$\Phi_{UP}(q) = \begin{bmatrix} (R_i d_{oi})^T \overline{QP} \\ (R_i d_{oj})^T \overline{QP} \\ (R_i d_{oi})^T (R_j d_{oj}) \end{bmatrix} = \mathbf{0}_{3 \times 1} \quad (12)$$

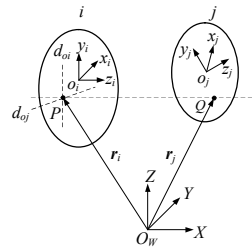


Figure 6. Constraint vector of the composite UP joint.

The polishing robot is actuated by three prismatic joints. The mechanism has three DOFs, allowing the three actuators to produce specific movements. To conduct dynamic analysis, the trajectory of the moving platform needs to be determined. Through kinematic analysis, the displacement curves $f_n(t)$ ($n = 1, 2, 3$) of the three actuators are determined, and the derivation of the driving constraint equation is presented as follows:

$$\Phi_D = \begin{bmatrix} |\rho_1 - \rho_5| - f_1(t) \\ |\rho_2 - \rho_6| - f_2(t) \\ |\rho_3 - \rho_7| - f_3(t) \end{bmatrix} = \mathbf{0}_{3 \times 1} \quad (13)$$

where ρ_i ($i = 1, 2, 3, 5, 6, 7$) denotes the vector position of U_i ($i = 1, 2, 3, 5, 6, 7$) in W -XYZ.

According to Equations (8)–(13), the complete constraint equation of the polishing parallel manipulator is as follows:

$$\Phi(q) = \begin{bmatrix} \Phi_{U1} & \Phi_{U2} & \Phi_{U3} & \Phi_{U5} & \Phi_{U6} & \Phi_{U7} & \Phi_{UP} \\ \Phi_{P1} & \Phi_{P2} & \Phi_{P3} & \Phi_{R1} & \Phi_{R2} & \Phi_{R3} & \Phi_D \end{bmatrix}^T = \mathbf{0}_{60 \times 1} \quad (14)$$

3.2. Dynamic Modeling with Joint Clearance

The constraint equation at the clearance is substituted with the contact force constraint, and the constraint equation corresponding to Equation (14) is removed. The constraint equation with prismatic joint clearance is derived as follows:

$$\Phi_s(q) = \begin{bmatrix} \Phi_{U1} & \Phi_{U2} & \Phi_{U3} & \Phi_{U5} & \Phi_{U6} & \Phi_{U7} & \Phi_U \\ \Phi_{P1} & \Phi_{P2} & \Phi_{P3} & \Phi_{R1} & \Phi_{R2} & \Phi_{R3} & \Phi_D \end{bmatrix}^T = \mathbf{0}_{60 \times 1} \quad (15)$$

Through the calculation of partial derivatives of Equation (14) in terms of t (time), the velocity and acceleration constraint equations of the system are solved as follows:

$$\Phi_{sq} \dot{q} = -\Phi_{st} = v \quad (16)$$

$$Q_{sq} \ddot{q} = -\left(Q_{sq} \dot{q}\right) \dot{q} - 2\Phi_{sq} \dot{q} - \Phi_{stt} = \gamma \quad (17)$$

where Φ_{sq} is the matrix of derivatives of the constraint equations in terms of the generalized coordinates q ; \dot{q} represents the first derivative of the generalized coordinate; Φ_{st} is the derivative of the constraint equation; v is the right side of the velocity constraint

equation; \ddot{q} is the generalized acceleration column vector; Φ_{sq} is the derivative matrix of the Jacobian matrix of the constraint equation; and γ is the right side of the acceleration constraint equation.

The dynamic equation of the 3-UPRU+UP parallel manipulator with Lagrange multipliers is obtained as follows:

$$M\ddot{q} + \Phi_{sq}^T \lambda = F \quad (18)$$

where M is the generalized mass matrix; λ is the Lagrange multiplier; $\Phi_{sq}^T \lambda$ is related to the joint constraint reaction force/torque and driving force/torque; and F is the generalized external forces.

By combining Equations (17) and (18), we can obtain the following dynamic equation:

$$\begin{pmatrix} M & \Phi_{sq}^T \\ \Phi_{sq} & 0 \end{pmatrix} \begin{pmatrix} \ddot{q} \\ \lambda \end{pmatrix} = \begin{pmatrix} F \\ \gamma \end{pmatrix} \quad (19)$$

When solving dynamic equations using integral methods, the accumulation of errors over time leads to growing constraint violations, which reduces the accuracy of the final results and may even produce incorrect outcomes. To improve this method, Baumgarte [22] applied the correction idea from control systems, making corrections in real time based on the violation of position and velocity constraints. Equation (19) can be rewritten as:

$$\begin{bmatrix} M & \Phi_{sq}^T \\ \Phi_{sq} & 0 \end{bmatrix} \begin{bmatrix} \ddot{q} \\ \lambda \end{bmatrix} = \begin{bmatrix} F \\ \gamma - 2\alpha_b \dot{\Phi}_s - \beta_b^2 \Phi_s \end{bmatrix} \quad (20)$$

where α_b and β_b are stability coefficients, and their values are selected from experience. $2\alpha_b \dot{\Phi}_s$ and $\beta_b^2 \Phi_s$ play the role of control terms. The function ode45 of the MATLAB method was used to integrate the differential equation of the 3-UPRU+UP parallel manipulator. When the Baumgarte parameters are taken $\alpha_b = 5$ and $\beta_b = 1$, the violation amount of the position constraint equation is below 1×10^{-10} m.

The dynamic simulation solution flowchart of the 3-UPRU+UP parallel manipulator considering the clearance joint is shown in Figure 7.

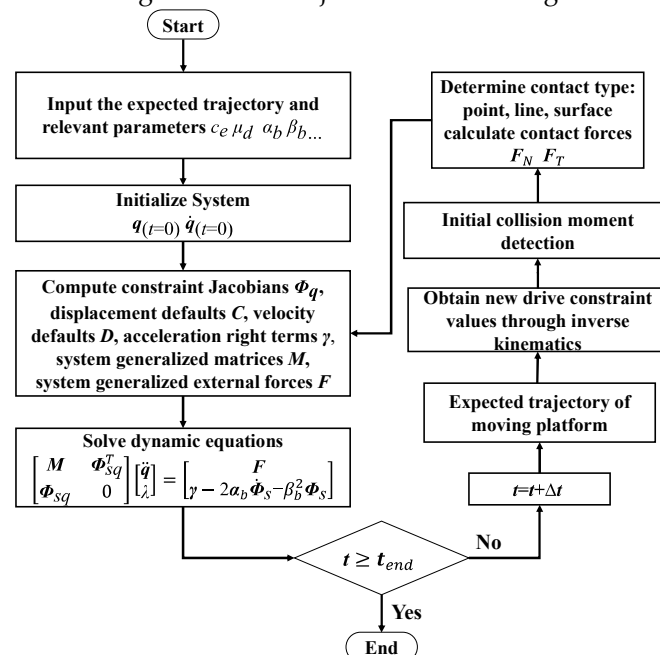


Figure 7. Dynamic simulation solution flowchart.

4. Dynamics Simulation

In the optical mirror processing process, the grinding tool, by a certain trajectory, speed, and acceleration, accurately traverses the mirror surface to be processed on each removal point; when the grinding trajectory is a circle, the grinding tool does not need to change direction frequently in the process of movement, and can make the grinding tool in the process of grinding processing and the mirror surface type match, suitable for the rotary symmetry class of optical component processing. This study examines the impact of joint clearance on the dynamic characteristics of a polishing robot by conducting motion trajectory planning for its moving platform as follows:

$$\begin{cases} X = X_c + r \cos(\theta_0 + \frac{vt}{r}) \\ Y = Y_c + r \sin(\theta_0 + \frac{vt}{r}) \\ Z = Z_0 \end{cases} \quad (21)$$

where (X_c, Y_c, Z_0) is the position of the center of the trajectory circle in W -XYZ, r is the radius of the trajectory circle with $r = 0.2$ m, θ_0 is the initial position of the center of the moving platform on the trajectory circle, and v is the linear velocity of the moving platform with $v = 0.05$ m/s.

The structural parameters and the dynamic simulation parameters are shown in Table 2 and Table 3, respectively.

Table 2. Structural parameters of the 3UPRU+UP parallel manipulator.

Parameter	Value
Mass of UP branched-chain and moving platform m_m /kg	138.239
Inertia matrix of UP branched-chain and moving platform J_m /kg·m ²	diag[35.509,35.478,1.452]
Circumcircle radius of universal joints U_i r_s /m	0.4
Circumcircle radius of universal joints U_k r_m /m	0.15
Length of cylinder block components $L_{a,i}$ /m	0.6
Mass of cylinder block components $m_{a,i}$ /kg	70.8
Inertia matrix of cylinder block component $J_{a,i}$ /kg·m ²	diag[14.264,14.598,0.203]
Length of telescopic rod components $L_{b,i}$ /m	1.2
Mass of telescopic rod components $m_{b,i}$ /kg	29.85
Inertia matrix of telescopic rod component $J_{c,i}$ /kg·m ²	diag[5.94,5.94,0.02]
Length of rotating rod components $L_{c,i}$ /m	0.09
Mass of rotating rod components $m_{c,i}$ /kg	1.3
Inertia matrix of rotating rod component $J_{c,i}$ /kg·m ²	diag[0.004,0.004,0.004]
External load/kg	118.5

Table 3. Dynamic simulation parameters.

Parameter	Value	Parameter	Value
Young's modulus	200 Gpa	static friction coefficient μ_s	0.80
Restitution coefficient c_e	0.9	sliding friction coefficient μ_d	0.16
Baumgarte α_b	5	MATLAB integration step	0.0001s
Baumgarte β_b	1	MATLAB integral function	ode45

The simulation time is 0.3 s, with an initial step size of 0.0001 s. The motion curves of the moving platform of the 3-UPRU+UP parallel manipulator are obtained through MATLAB numerical solution and ADAMS simulation. Figure 8 shows that the MATLAB and ADAMS curves share a similar overall kinematic trend. However, due to different

solution methods and modeling approaches in MATLAB and ADAMS, the gap simulations are random. This results in varying initial collision positions and peak times for collision forces. If the mechanism is stable, the two curves will be nearly identical, thus validating the selected dynamic model once more.

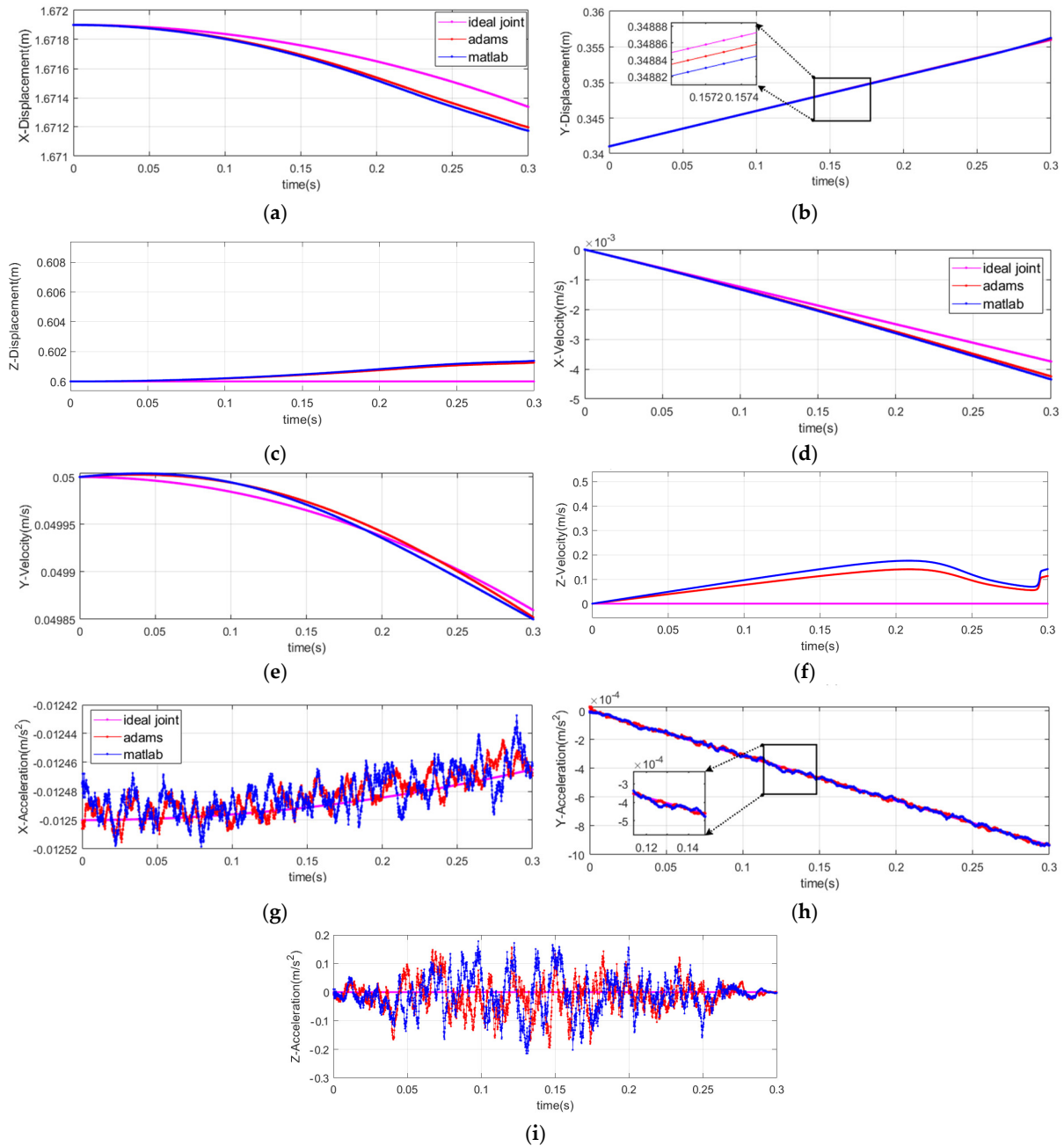


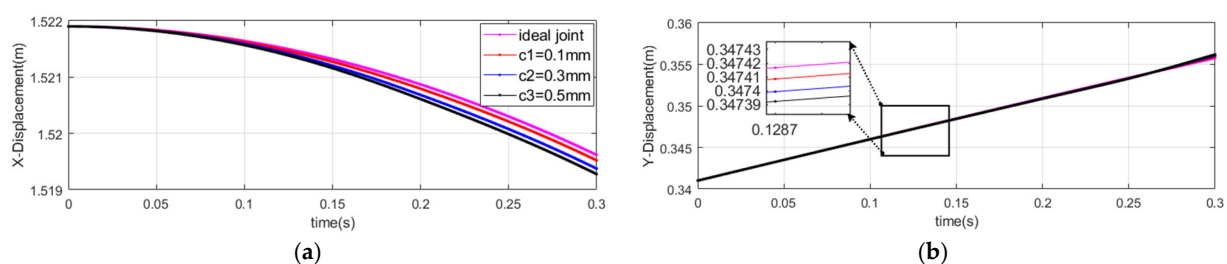
Figure 8. Dynamic responses of the moving platform with clearance: (a–c) displacement, (d–f) velocity, (g–i) acceleration.

As shown in Figure 8a–c, during the operation of the robot, the joint clearance can lead to displacement errors due to the separation of the elements. Clearance joints have a negligible effect on the displacement of the moving platform: a joint clearance of 0.01 mm results in a displacement error of 0.1 mm. Figure 8d–f shows the velocity of the moving platform. The effect of the joint clearance on velocity is more pronounced than its effect on displacement, being an order of magnitude greater. The velocity swings sharply around the ideal curve due to sudden changes in acceleration. As shown in Figure 8g–i, when joint clearance is present, the acceleration curve exhibits high-frequency

fluctuations, indicating that clearance has the most pronounced effect on the acceleration of the parallel manipulator. The acceleration undergoes a sudden change. This is caused by the joint clearance resulting in collision and friction between the guide and the slider. The sudden change in friction and contact force indicates that the contact between the elements has altered, consistent with the results of the point–line–surface contact model used earlier.

After a long period of operation of the mechanism, the joints are subjected to wear and tear phenomena, which lead to a larger clearance size. Therefore, it is necessary to investigate the effect of clearance size on the dynamics of the mechanism. The displacement, velocity, and acceleration curves for the moving platform are plotted. As shown in Figure 9a–c, when the clearance size gets larger, the displacement error of the moving platform becomes more significant. The displacement in X and Y directions of the moving platform is basically unchanged, but the displacement deviation in Z direction becomes larger, and the displacement deviation in Z direction is 1.6 mm, 3.3 mm, and 5.4 mm, respectively, with the increase in clearance. By comparing Figure 9d–f, it is evident that, with the growth in the clearance size, the fluctuations in the velocity curve become more conspicuous. Z-direction vibration amplitude is relatively large, 0.15, 0.19, and 0.26 m/s, respectively. As shown in Figure 9g–i, the clearance has a large effect on the acceleration of the moving platform. The larger the clearance is, the larger the acceleration peak is, and the amplitude of the sudden change in acceleration in the Z direction is 0.21, 0.32, and 0.61 m/s^2 , respectively. This results in greater vibration and instability during the operation of the mechanism. The reason behind this is that the enlarged gap size causes frequent alterations in the contact state between the slider and the guideway. Moreover, the fluctuations and amplitudes of the clearance collision force increase, thus influencing the stability of the mechanism's movement.

Collision and sliding at the gap inevitably generate friction. Figure 10 shows the dynamic response of the parallel manipulator with friction coefficients of 0.02, 0.05, and 0.08, and a clearance of 0.1 mm is simulated and solved. As shown in Figure 10a–c, when the clearance size gets larger, the displacement error of the moving platform becomes more significant, and the displacement of the moving platform in X and Y directions is very small, but the displacement deviation in Z direction becomes larger, and, with the increase in clearance, the displacement deviation in Z direction is 2.2 mm, 3.3 mm, and 5.4 mm, respectively. As shown in Figure 10d–f, it can be seen that, with the increase in the friction factor, the vibration amplitude changes slightly, and the Z-direction vibration amplitude is relatively large, the Z-direction amplitude being 0.08, 0.13, and 0.20 m/s, respectively. From Figure 10g–i, it can be observed that the friction factor has a large influence on the acceleration of the moving platform, the fluctuation amplitude of the acceleration curve changes with the change in the friction factor, and the fluctuation amplitude of the acceleration curve in the Z direction is 0.19, 0.32, and 0.42 m/s^2 , respectively. Contact force in prismatic joints increases with increasing coefficient of friction. As depicted in Figure 11, it attains a maximum value of 408 N, which has a substantial impact on the stable operation of the mechanism.



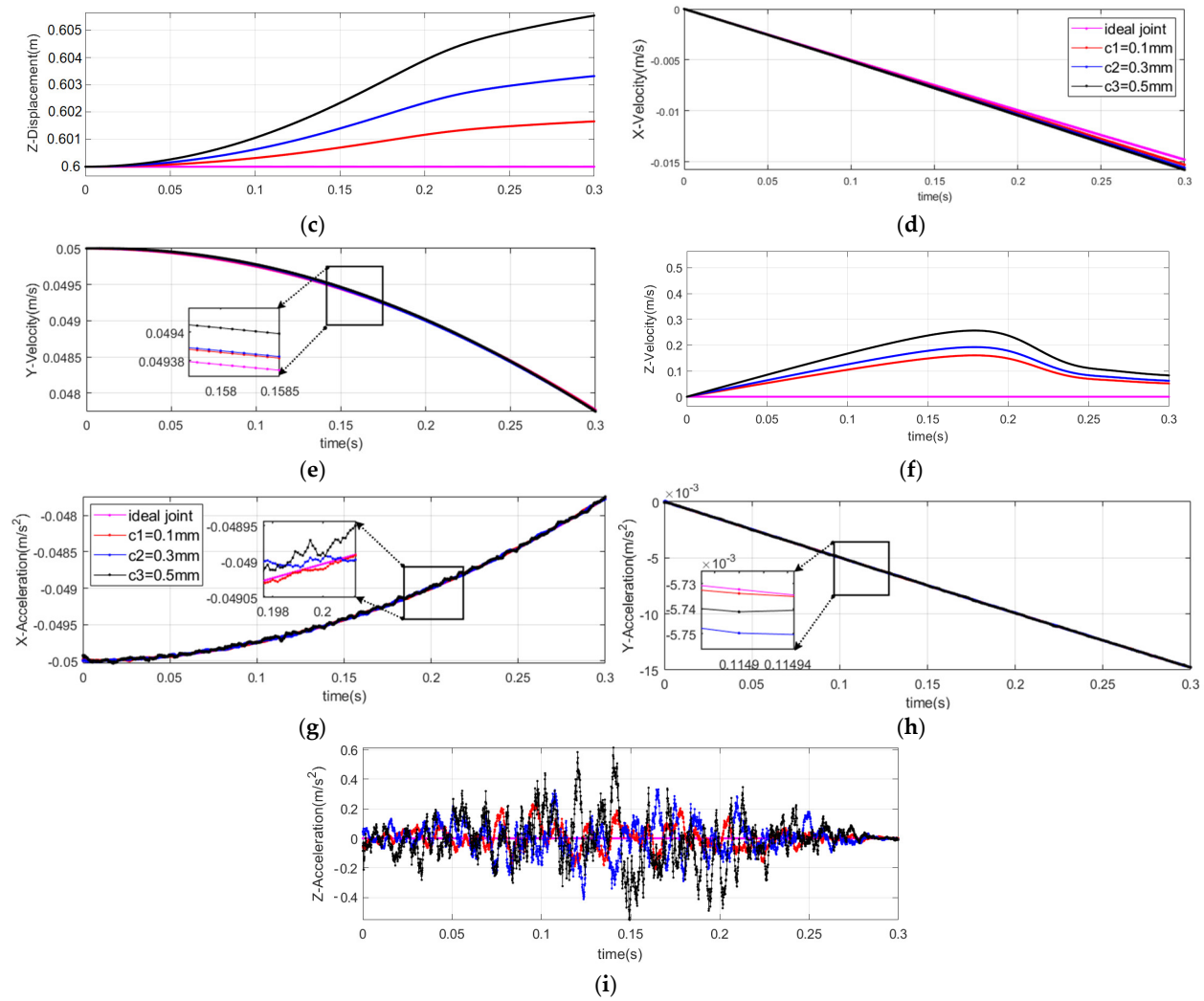
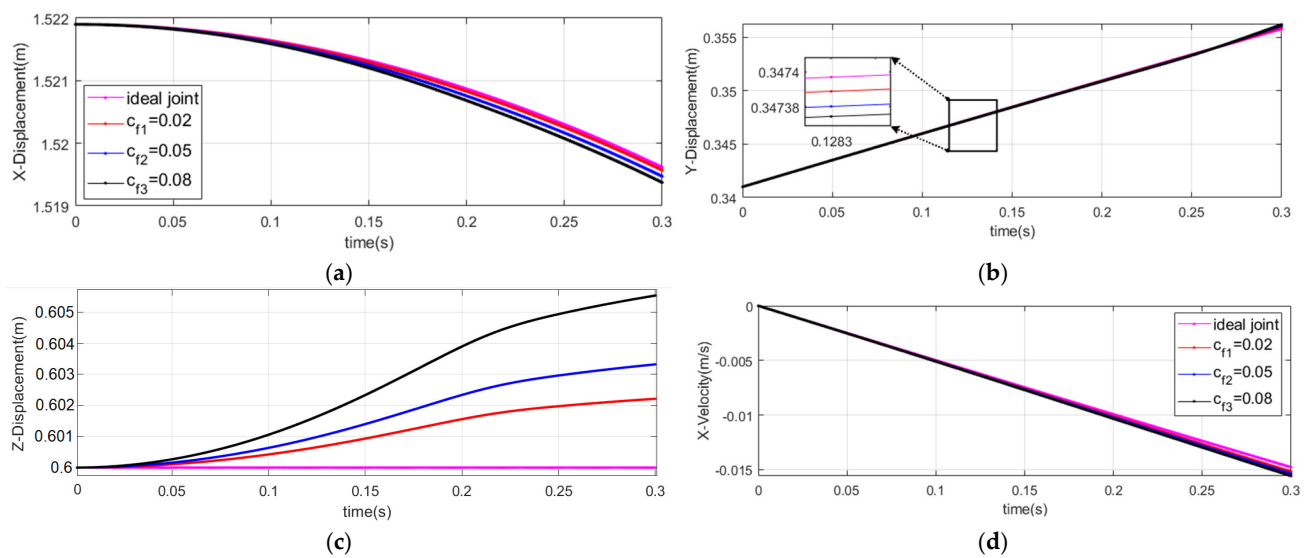


Figure 9. Dynamic responses of the moving platform with different clearance sizes: (a–c) displacement, (d–f) velocity, (g–i) acceleration.



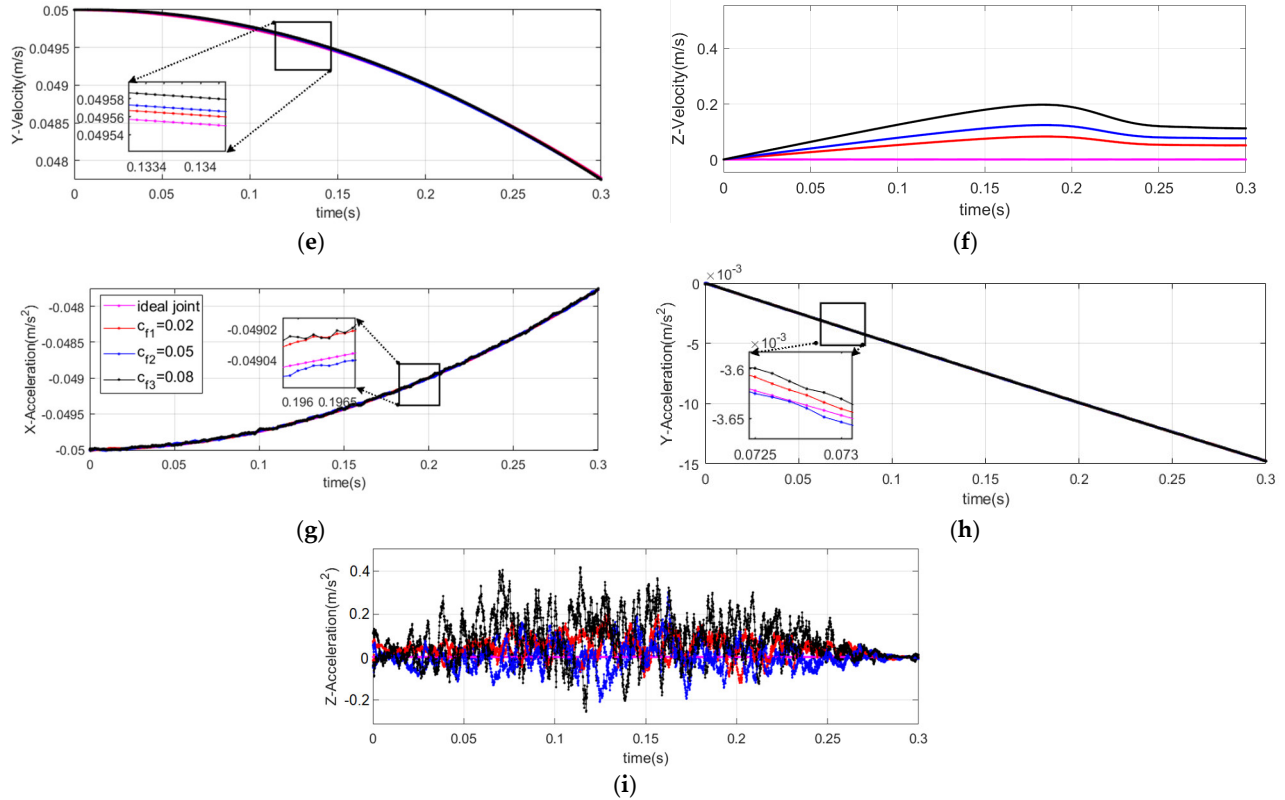


Figure 10. Dynamic responses of the moving platform with different friction coefficients: (a–c) displacement, (d–f) velocity, (g–i) acceleration.

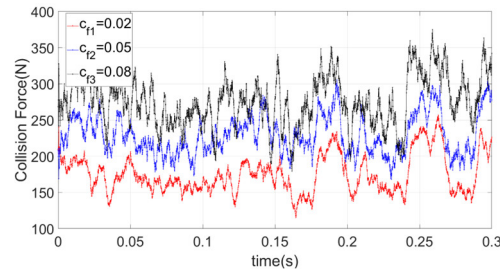


Figure 11. Contact forces in prismatic joint.

5. Discussion

The research presented in this study significantly contributes to the field of robotic dynamics, particularly for optical machining robots with prismatic joint clearances. By modeling the dynamics of a space-parallel robot with joint clearances, the simulation results demonstrate that the effects of clearances on the moving platform's dynamics align with previous literature: joint clearances significantly impact the robot's dynamics and must be compensated for and controlled through specific measures. Additionally, the current model incorporates certain simplifications in joint contact mechanics and material properties. Future work could explore more complex contact modeling and experimental validation to enhance the accuracy of dynamic predictions.

6. Conclusions

In this paper, a method for modeling parallel manipulators with prismatic joint clearances is presented, and this method is based on the LMD. Firstly, a simplified prismatic joint model is used to describe 15 different point–line–surface contact modes between the slider and the guide rail, and formulas for contact and friction forces in different contact

modes are provided. Then, based on the LMD, constraint equations for four typical joints are given, and the dynamic model of the 3-UPRU+UP parallel manipulator with prismatic joint clearance is derived. Numerical calculations are carried out using ADAMS and MATLAB to verify the correctness of the dynamic model. Finally, the dynamic responses of the robot under different joint clearance sizes and different friction factors are obtained, and it is found that the impact of clearance on the robot's dynamics becomes more significant as the clearance increases.

This study provides a theoretical reference for the joint design of parallel manipulators and for compensating for the gap effect through algorithms.

Author Contributions: Conceptualization, S.Z.; methodology, S.Z., G.C., F.G., and Y.P.; formal analysis, S.Z., G.C., and F.G.; writing—original draft preparation, S.Z.; writing—review and editing, G.C., F.G., and Y.P.; project administration, G.C. All authors have read and agreed to the published version of the manuscript.

Funding: This study was financially supported by the National Natural Science Foundation of China (Grant No. 52275039) and the Natural Science Program of Jiangsu College of Safety Technology (Grant No. 145892024ZY02).

Institutional Review Board Statement: Not applicable.

Informed Consent Statement: Not applicable.

Data Availability Statement: The simulation and experimental data used to support the findings of this study are available from the corresponding author upon request.

Conflicts of Interest: The authors declare no conflicts of interest.

References

1. Feng, H.; Huang, L.; Huang, P.; Liu, J.; He, X.; Peng, Y. Review on high efficiency and high precision compliant polishing method. *Int. J. Adv. Manuf. Technol.* **2024**, *132*, 2091–2128. <https://doi.org/10.1007/s00170-024-13388-z>.
2. Jin, Z.; Yin, Z.; Liu, H.; Liu, F. Dynamic Characteristics, Analysis, and Measurement of a Large Optical Mirror Processing System. *Machines* **2024**, *12*, 788. <https://doi.org/10.3390/machines12110788>.
3. Erkaya, S.; Doğan, S.; Ulus, Ş. Effects of joint clearance on the dynamics of a partly compliant mechanism: Numerical and experimental studies. *Mech. Mach. Theory* **2015**, *88*, 125–140. <https://doi.org/10.1016/j.mechmachtheory.2015.02.007>.
4. Varedi-Koulaei, S.M.; Daniali, H.M.; Farajtabar, M.; Fathi, B.; Shafiee-Ashtiani, M. Reducing the undesirable effects of joints clearance on the behavior of the planar 3-RRR parallel manipulators. *Nonlinear Dyn.* **2016**, *86*, 1007–1022. <https://doi.org/10.1007/s11071-016-2942-7>.
5. Li, B.; Wang, M.S.; Gantes, C.J.; Tan, U.X. Modeling and simulation for wear prediction in planar mechanical systems with multiple clearance joints. *Nonlinear Dyn.* **2022**, *108*, 887–910. <https://doi.org/10.1007/s11071-022-07224-w>.
6. Ren, J.; Zhang, J.; Wei, Q. Dynamic analysis of planar four-bar mechanism with clearance in microgravity environment. *Nonlinear Dyn.* **2024**, *112*, 15933–15951. <https://doi.org/10.1007/s11071-024-09874-4>.
7. Ma, J.; Qian, L. Modeling and simulation of planar multibody systems considering multiple revolute clearance joints. *Nonlinear Dyn.* **2017**, *90*, 1907–1940. <https://doi.org/10.1007/s11071-017-3771-z>.
8. Erkaya, S.; Dogan, S.; Sefkatlioglu, E. Analysis of the joint clearance effects on a compliant spatial mechanism. *Mech. Mach. Theory* **2016**, *104*, 255–273. <https://doi.org/10.1016/j.mechmachtheory.2016.06.009>.
9. Chen, X.L.; Li, Y.W.; Jia, Y.H. Dynamic Response and Nonlinear Characteristics of Spatial Parallel Mechanism With Spherical Clearance Joint. *J. Comput. Nonlinear Dyn.* **2019**, *14*, 041010. <https://doi.org/10.1115/1.4042636>.
10. Cretescu, N.; Neagoe, M.; Saulescu, R. Dynamic Analysis of a Delta Parallel Robot with Flexible Links and Joint Clearances. *Appl. Sci.* **2023**, *13*, 6693. <https://doi.org/10.3390/app13116693>.
11. Wang, S.P.; Cui, Y.; Wang, C.E. Dynamics Analysis and Chaos Identification of Compound Pendulum Jaw Crusher with Joint Clearance. *Appl. Sci.* **2023**, *13*, 238. <https://doi.org/10.3390/app13010238>.
12. Wang, Y.; Li, R.; Liu, J.; Jia, Z.; Liang, H. Dynamic Characteristics Analysis of an Assembly Robot for a Wine Box Base Considering Radial and Axial Clearances in a 3D Revolute Joint. *Appl. Sci.* **2023**, *13*, 2211. <https://doi.org/10.3390/app13042211>.

13. Qian, M.B.; Qin, Z.; Yan, S.Z.; Zhang, L. A comprehensive method for the contact detection of a translational clearance joint and dynamic response after its application in a crank-slider mechanism. *Mech. Mach. Theory* **2020**, *145*, 103717. <https://doi.org/10.1016/j.mechmachtheory.2019.103717>.
14. Qi, Z.H.; Luo, X.M.; Huang, Z.H. Frictional contact analysis of spatial prismatic joints in multibody systems. *Multibody Syst. Dyn.* **2011**, *26*, 441–468. <https://doi.org/10.1007/s11044-011-9264-9>.
15. Shiau, T.N.; Tsai, Y.J.; Tsai, M.S. Nonlinear dynamic analysis of a parallel mechanism with consideration of joint effects. *Mech. Mach. Theory* **2008**, *43*, 491–505. <https://doi.org/10.1016/j.mechmachtheory.2007.03.008>.
16. Qian, M.; Qin, Z.; Yan, S.; Zhang, L. Contact force analysis in a planar mechanism with translational clearance joint considering complex contact modes. *IOP Conf. Series Mater. Sci. Eng.* **2019**, *657*, 012059.
17. Mostaghel, N.; Davis, T. Representations of Coulomb Friction for Dynamic Analysis. *Earthq. Eng. Struct. Dyn.* **1997**, *26*, 541–548.
18. Cornec, A.; Lilleodden, E. Stress-strain curve estimation from micropillar compression with transverse contraction effect. *Mater. Today Commun.* **2024**, *41*, 110396. <https://doi.org/10.1016/j.mtcomm.2024.110396>.
19. Pereira, C.; Ramalho, A.; Ambrosio, J. Applicability domain of internal cylindrical contact force models. *Mech. Mach. Theory* **2014**, *78*, 141–157. <https://doi.org/10.1016/j.mechmachtheory.2014.03.010>.
20. Puttock, M.J.; Thwaite, E.G. *Elastic Compression of Spheres and Cylinders At Point and Line Contact*; Commonwealth Scientific and Organization: Melbourne, Australia, 1969.
21. Ma, J.; Qian, L.; Chen, G. Parameter estimation of the Lankarani-Nikravesh contact force model using a new modified linear method. In Proceedings of the 2015 IEEE International Conference on Advanced Intelligent Mechatronics (AIM), Busan, Republic of Korea, 7–11 July 2015; pp. 494–499. <https://doi.org/10.1109/AIM.2015.7222582>.
22. Flores, P.; Machado, M.; Seabra, E.; Tavares da Silva, M. A Parametric Study on the Baumgarte Stabilization Method for Forward Dynamics of Constrained Multibody Systems. *J. Comput. Nonlinear Dyn.* **2011**, *6*, 011019. <https://doi.org/10.1115/1.4002338>.

Disclaimer/Publisher’s Note: The statements, opinions and data contained in all publications are solely those of the individual author(s) and contributor(s) and not of MDPI and/or the editor(s). MDPI and/or the editor(s) disclaim responsibility for any injury to people or property resulting from any ideas, methods, instructions or products referred to in the content.